Research

CrossMark
click for updates

Author for correspondence:

F. Mellibovsky

e-mail:

fernando.mellibovsky@upc.edu

Mean structure of the supercritical turbulent spiral regime in Taylor-Couette flow

B. Wang[1], F. Mellibovsky[1], R. Ayats[2], K. Deguchi[3] and A. Meseguer[1]

[1]Departament de Física, Universitat Politècnica de Catalunya, 08034, Barcelona, Spain
[2]Institute of Science and Technology Austria (ISTA), 3400 Klosterneuburg, Austria
[3]School of Mathematics, Monash University, VIC 3800, Australia

The large-scale laminar/turbulent spiral patterns that appear in the linearly unstable regime of counter-rotating Taylor-Couette flow are investigated from a statistical perspective by means of direct numerical simulation. Unlike the vast majority of previous numerical studies, we analyse the flow in periodic parallelogram-annular domains, following a coordinate change that aligns one of the parallelogram sides with the spiral pattern. The domain size, shape and spatial resolution have been varied and the results compared with those in a sufficiently large computational orthogonal domain with natural axial and azimuthal periodicity. We find that a minimal parallelogram of the right tilt significantly reduces the computational cost without noticeably compromising the statistical properties of the supercritical turbulent spiral. Its mean structure, obtained from extremely long time integrations in a corotating reference frame using the method of slices, bears remarkable similarity with the turbulent stripes observed in plane Couette flow, the centrifugal instability playing only a secondary role.

1. Introduction

Fluid flow intermittency, i.e. the spatio-temporal coexistence of laminar and turbulent flow regions, remains one of the most intriguing phenomena in fluid dynamics. Intermittency arises frequently in the transitional regime of a wide variety of canonical shear flow problems.

THE ROYAL SOCIETY
PUBLISHING

In pipe or channel flows, it typically shows in the form of localised turbulent patches (customarily dubbed *puffs* or *spots*), flanked by laminar quiescent flow. For a thorough review on the rich variety of existing intermittent shear flow phenomena, see [1] and references therein.

Interestingly, in some cases, as the turbulent fraction grows upon increasing the Reynolds number, the spots rearrange in oblique turbulent bands or stripes that exhibit sharp interfaces at a clear-cut tilt with respect to the main direction of the flow. A paradigm of banded intermittency arises in counter-rotating Taylor-Couette flow (TCF), i.e. the fluid flow between independently-rotating coaxial cylinders [2]. First discovered by Coles & Van Atta [3] in the 1960s, the *Spiral Turbulence* regime (SPT) consists of a rotating helical pattern of alternated turbulent and laminar stripes. This peculiar flow structure has since puzzled fluid dynamicists, physicists and the scientific community in general [4]. It was not until the late 2000s that SPT could finally be reproduced numerically by means of direct numerical simulation (DNS) [5–8], but the underlying flow mechanisms remain still poorly understood.

For reasons that we shall discuss below, the main testing ground for turbulent stripe analysis has mostly shifted to parallel flows, notably plane Couette flow (PCF) [9,10]. As a result, while DNS of parallel flows has already satisfactorily revealed in detail the mean properties of turbulent stripes [1], the numerical analysis of SPT in TCF trails many years behind.

Given the statistical invariance of laminar/turbulent banded patterns along the stripe direction, narrow rectangular computational domains, suitably tilted to align with the pseudo-periodic pattern, have been used in cartesian geometries to curtail the computational burden [11–14]. The task is straightforwardly undertaken for parallel shear flows by simply skewing the base flow direction, but annular geometries demand essential modification of the numerical formulation. The coordinate change that accomplishes this was first proposed by [15,16] with the aim of computing mixed-mode TCF travelling-rotating waves as relative equilibria in minimal domains. To the best of our knowledge, the generalisation of this coordinate change to allow DNS in parallelogram-annular-shaped domains had not been attempted until very recently [17], despite its being absolutely requisite to the efficient computation of SPT dynamics.

An additional difficulty that plagues the SPT regime in TCF, and concerns also the laminar-turbulent stripes observed in PCF, is the drift of flow structures induced by the completely broken streamwise symmetry (note that PCF retains a streamwise reflection symmetry in the form of a composition with cross-stream reflection). This hinders the otherwise straightforward extraction of the statistical large-scale structure of the banded pattern. A meaningful computation of mean and root mean square (rms) fields requires the definition of a suitable frame of reference that drifts with the flow structure of interest. A powerful tool to achieve this is provided by the method of slices [18,19], which allows quotienting out the trivial drift dynamics along group orbits associated with homogeneous space directions.

Moreover, SPT occurs in both the subcritical and supercritical parameter-space regions of TCF. Subcritical SPT is qualitatively analogous to the laminar/turbulent patterns that arise in linearly stable parallel flows such as PCF, and has therefore been the subject of much research. Meanwhile, supercritical SPT, the focus here, has hitherto not been given much attention despite its practical interest from the standpoint of competing shear and Coriolis forces. This interaction is at the origin of large-scale coherent structures arising, as a relevant example, in geophysical flows, SPT playing an archetypal role. In the early supercritical regime, before SPT sets in, the flow is governed by a dislocated pattern of laminar spirals (SPI) that fills the centrifugally unstable region of the annulus [20,21].

The DNS of laminar-turbulent banded patterns in extended shear flows such as SPT generally requires discretising the Navier-Stokes equations in overly large computational domains, as their oblique arrangement calls for long spanwise and streamwise periodicities even for a minimal representation. Early numerical computations on SPT were therefore forced to sacrifice, to some extent, spatial resolution in exchange for feasibility [5–7]. We will show that these studies can no longer be considered sufficiently accurate by current standards. Especially if the focus is set on the statistical properties of turbulence. Converging mean and rms statistics of velocity fields requires

3

rsta.royalsocietypublishing.org Phil. Trans. R. Soc. A 0000000

very well-resolved spatio-temporal scales and long time integrations, such that optimising the computational cost through a convenient minimal choice of the domain is an essential step towards undertaking comprehensive parameter explorations of SPT.

Our aim here is threefold. First, we set out to produce a highly accurate computation of supercritical SPT in the minimal ordinary periodic-orthogonal-annular domain that can contain it. The data set thus generated is not only valuable for the analysis of the supercritical SPT regime, but also as a numerical benchmark for future analysis. Next, we switch to the parallelogram-annular domain shape with the purpose of exploiting its versatility in finding something akin to the *minimal flow unit* often used for the analysis of coherent structures in shear flow turbulence [22,23], but aiming instead at retaining also the large-scale features of intermittency, including its statistical properties. Finally, we compare the mean large-scale structure of SPT, computed in the co-rotating reference frame through the slicing technique [19], with that of turbulent stripes in PCF [9].

The paper is structured as follows. In section §2 we briefly present the formulation and describe the numerical methods employed. The supercritical SPT regime and the specific choice of geometric and flow parameters used in its obtention are provided in section §3, along with a demonstration of the capabilities of the parallelogram domain when combined with the method of slices. A thorough numerical convergence analysis varying domain size, shape, and spatial resolution, is then carried out in section §4, followed by the statistical description of SPT and the analysis of its mean large-scale structure in section §5. Finally, the main results are summarised and conclusions drawn in section §6.

2. Formulation and methods

Consider the incompressible flow of a fluid of dynamic viscosity μ and density ϱ (kinematic viscosity $\nu = \mu/\varrho$) completely filling the gap between two concentric and independently-rotating cylinders, whose inner and outer radii and angular velocities are r_i^*, r_o^* and Ω_i, Ω_o, respectively. The dynamics is governed by the Navier–Stokes equations, which, after convenient non-dimensionalisation with the gap $d = r_o^* - r_i^*$ and d^2/ν as units for space and time, read

$$\partial_t \mathbf{v} + (\mathbf{v} \cdot \nabla)\mathbf{v} = -\nabla p + \nabla^2 \mathbf{v} + \mathcal{F}\,\hat{\boldsymbol{z}}, \tag{2.1}$$

$$\nabla \cdot \mathbf{v} = 0. \tag{2.2}$$

The axial forcing term $\mathcal{F} = \mathcal{F}(t)$ in (2.1) is instantaneously adjusted to enforce the zero axial net massflux condition at all times, and $p = p(r,\theta,z;t)$ and $\mathbf{v} = \mathbf{v}(r,\theta,z;t) = (v_r, v_\theta, v_z) = v_r\,\hat{\boldsymbol{r}} + v_\theta\,\hat{\boldsymbol{\theta}} + v_z\,\hat{\boldsymbol{z}}$ are the dimensionless reduced pressure and velocity, respectively, expressed in cylindrical coordinates (r, θ, z). The velocity must satisfy no-slip boundary conditions at the cylinder walls and zero axial net massflux

$$\mathbf{v}|_{r=r_i} = (0, \mathrm{R_i}, 0), \quad \mathbf{v}|_{r=r_o} = (0, \mathrm{R_o}, 0), \quad Q(\mathbf{v}) = \int_0^{2\pi} \int_{r_i}^{r_o} (\mathbf{v} \cdot \hat{\boldsymbol{z}})\, r\, dr\, d\theta = 0, \tag{2.3}$$

where $r_i = r_i^*/d = \eta/(1-\eta)$ and $r_o = r_o^*/d = 1/(1-\eta)$, with $\eta = r_i^*/r_o^*$ the radius ratio, and $\mathrm{R_i} = dr_i^*\Omega_i/\nu$ and $\mathrm{R_o} = dr_o^*\Omega_o/\nu$ are the inner and outer cylinder Reynolds numbers. The basic, laminar and steady *circular Couette flow*, henceforth referred to as CCF, is

$$\mathbf{v}_b = v_\theta^b(r)\,\hat{\boldsymbol{\theta}}, \quad p_b(r) = \int \frac{(v_\theta^b)^2}{r}\, dr, \quad f_b = 0, \tag{2.4}$$

with $v_\theta^b = r(\mathrm{R_o} - \eta\mathrm{R_i})(1+\eta)^{-1} + \eta(\mathrm{R_i} - \eta\mathrm{R_o})(1-\eta)^{-1}(1-\eta^2)^{-1}r^{-1}$. The perturbation velocity and pressure fields are defined as

$$\mathbf{u}(r,\theta,z;t) = \mathbf{v}(r,\theta,z;t) - \mathbf{v}_b(r) = u_r\,\hat{\boldsymbol{r}} + u_\theta\,\hat{\boldsymbol{\theta}} + u_z\,\hat{\boldsymbol{z}}, \quad q(r,\theta,z;t) = p(r,\theta,z;t) - p_b(r). \tag{2.5}$$

Formal substitution of (2.5) into (2.1)-(2.2) shows that the perturbation fields must satisfy

$$\partial_t \mathbf{u} = -\nabla q + \nabla^2 \mathbf{u} - (\mathbf{v}_b \cdot \nabla)\mathbf{u} - (\mathbf{u} \cdot \nabla)\mathbf{v}_b - (\mathbf{u} \cdot \nabla)\mathbf{u} + \mathcal{F}\,\hat{\mathbf{z}} \tag{2.6}$$

$$\nabla \cdot \mathbf{u} = 0, \tag{2.7}$$

with $\mathbf{u}$ obeying homogeneous boundary conditions at the walls, $\mathbf{u}(r_i, \theta, z; t) = \mathbf{u}(r_o, \theta, z; t) = \mathbf{0}$, and satisfying the zero net axial mass flux condition, $Q(\mathbf{u}) = 0$.

Although this solenoidal boundary value problem is most naturally formulated in cylindrical polar coordinates (r, θ, z), many flow regimes involving spirals and/or mixed modes admit a much simpler and more economical numerical representation employing the oblique coordinates

$$\xi = n_1\theta + k_1 z, \quad \zeta = n_2\theta + k_2 z. \tag{2.8}$$

In this expression, the generalised wavenumber quadruplet (n_1, k_1, n_2, k_2) defines uniquely the orientation of, and periodicity along, the new coordinate axes (ξ, ζ).

The numerical discretisation of the boundary value problem (2.6-2.7) is accomplished with the solenoidal Petrov-Galerkin scheme originally formulated by [24], and suitably adapted to the annular-parallelogram domain $(r, \xi, \zeta) \in [r_i, r_o] \times [0, 2\pi] \times [0, 2\pi]$ by [17]. This discretisation implicitly assumes 2π-periodicity of both the pressure q and velocity $\mathbf{u}$ perturbation fields in the new ξ and ζ coordinates. In this transformed domain, the solenoidal velocity perturbation is approximated by means of a Fourier $\times$ Fourier $\times$ Chebyshev spectral expansion $\mathbf{u}_s$ of order $L \times N \times M$ in $\zeta \times \xi \times r$, respectively, of the form

$$\mathbf{u}_s(r, \xi, \zeta; t) = \sum_{\ell=-L}^{L} e^{i\ell\zeta} \sum_{n=-N}^{N} e^{in\xi} \underbrace{\sum_{m=0}^{M} a_{\ell n m}^{(1)}(t)\mathbf{u}_{\ell n m}^{(1)}(r) + a_{\ell n m}^{(2)}(t)\mathbf{u}_{\ell n m}^{(2)}(r)}_{\mathbf{u}_{\ell n}(r; t)}, \tag{2.9}$$

with $\mathbf{u}_{\ell n}$ the velocity field associated with the Fourier $\times$ Fourier mode (ℓ, n). The specific radial structure of the various $\mathbf{u}_{\ell n m}^{(\imath)}(r)$ for each quadruplet $(\ell, n, m, \imath)$ must be chosen so that the perturbation velocity field satisfies both the divergence-free (2.7) and the homogeneous Dirichlet boundary conditions. The resulting solenoidal, boundary-condition-compliant basis, as well as its dual counterpart, are an adaptation of those originally proposed by [24] for ordinary orthogonal domains, and may be found in [17], along with a detailed account of how formal substitution of the spectral expansion (2.9) into (2.6), followed by Hermitian projection onto each one of the dual basis elements, leads to a nonlinear system of ordinary differential equations for the $2 \times (2L + 1) \times (2N + 1) \times (M + 1)$ expansion coefficients $a_{\ell n m}^{(\imath)}(t)$. This system we integrate in time by means of a fourth-order linearly-implicit Backwards Differentiation scheme with explicit polynomial extrapolation of the nonlinear terms, conveniently started with a fourth order Runge-Kutta method. The factor 2 in the count of unknowns and the binary superindex $\imath = \{1, 2\}$ are the result of the solenoidal condition reducing from three to two the number of effective degrees of freedom per grid point.

We will characterise flows by their associated *normalised kinetic energy* κ of the perturbation velocity field, and by the corresponding inner and outer cylinders *normalised torque*, τ_i and τ_o,

$$\kappa = \frac{E(\mathbf{u})}{E(\mathbf{v}_b)}, \qquad \tau_{i,o} = 1 + \left.\frac{\partial_r(r^{-1}\langle u_\theta \rangle_{\xi\zeta})}{\partial_r(r^{-1}v_\theta^b)}\right|_{r=r_i, r_o}, \tag{2.10}$$

where

$$E(\mathbf{v}) = \frac{1}{2\mathcal{V}} \iiint_{\mathcal{V}} \mathbf{v} \cdot \mathbf{v} \, d\mathcal{V} = \frac{1}{2\mathcal{V}} \int_0^{2\pi} \int_0^{2\pi} \int_{r_i}^{r_o} \mathbf{v} \cdot \mathbf{v} \, r \, dr d\xi d\zeta = \frac{1-\eta}{1+\eta} \int_{r_i}^{r_o} \langle \mathbf{v} \cdot \mathbf{v} \rangle_{\xi\zeta} \, r \, dr \tag{2.11}$$

is the volume-averaged kinetic energy of some velocity field $\mathbf{v}$. The volume of the transformed computational domain is $\mathcal{V} = 2\pi^2(r_o^2 - r_i^2) = 2\pi^2(1-\eta)/(1+\eta)$, and $\langle\ \rangle_{\xi\zeta}$ implies averaging in both parallelogram directions. With these definitions, $\kappa = 0$ and $\tau_i = \tau_o = 1$ for CCF.
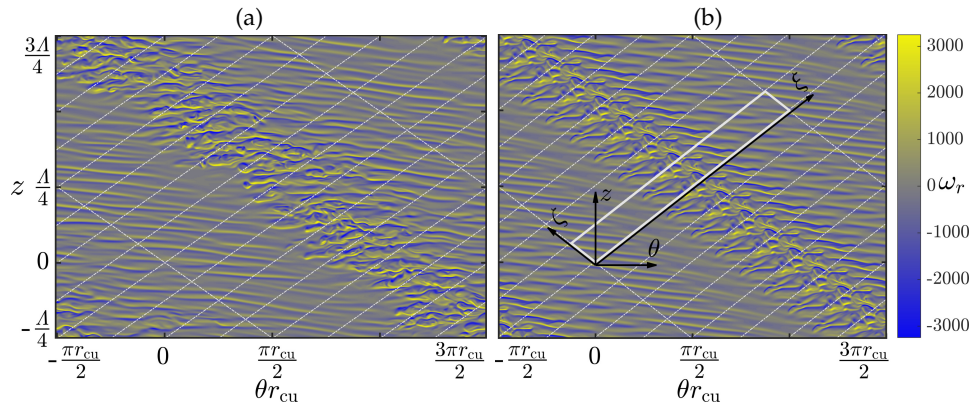
Figure 1. The SPT regime for $(\eta, \mathrm{R_i}, \mathrm{R_o}) = (0.883, 600, -1200)$, with $(\hat{n}, \hat{k}) = (1, 0.2)$. Instantaneous radial vorticity (ω_r) fields on a $\theta r - z$ section at $r = r_{\mathrm{cu}}$ as computed in (a) the full orthogonal domain $(n_1, k_1, n_2, k_2) = (1, 0.0, 0, 0.2)$ (See online movie), and (b) the parallelogram-shaped domain $(n_1, k_1, n_2, k_2) = (1, 0.2, -8, 1.6)$. The thin white lines demarcate the tessellation of the parallelogram domain (thick white).

3. Computational domains and the co-rotating reference frame

Throughout this study, we focus on the computation of the supercritical turbulent spiral known to arise at $(\mathrm{R_i}, \mathrm{R_o}) = (600, -1200)$ in an apparatus with $\eta = 0.883$ ($r \in [r_i, r_o] = [7.547, 8.547]$), and with an azimuthal-axial wavenumber pair $(\hat{n}, \hat{k}) = (1, 0.2)$ [5,17]. At these parameter values, CCF is subject to a centrifugal instability that is confined to the immediate neighbourhood of the inner cylinder ($r < r_n \simeq 7.867$, where $v_\theta^b(r_n) = 0$). The natural azimuthal periodicity of the spiral is $2\pi/\hat{n} = 2\pi$ and the imposed axial periodicity $\varLambda = 2\pi/\hat{k} = 31.416$, such that $\hat{n}/\hat{k} = 5$, which measures its slope, emulates the natural tilt selection observed in experiments [20].

In order to simulate the SPT regime in an ordinary orthogonal domain, a minimal choice for the generalised wavenumbers in (2.8) is $(n_1, k_1, n_2, k_2) = (\hat{n}, 0.0, 0, \hat{k}) = (1, 0.0, 0, 0.2)$. Figure 1a reproduces the computation of [5], but with a much higher spatial resolution of $(L, N, M) = (324, 324, 42)$, as required for statistical accuracy, and a time step $\varDelta t = 8 \times 10^{-6}$. The colour map shows the instantaneous radial vorticity (ω_r) field on an *unrolled* $\theta r - z$ section at $r = r_{\mathrm{cu}} = (r_i + r_n)/2 = 7.705$, in the midst of the *centrifugally unstable* region that characterises CCF at these values of the parameters. A well-defined stripe of turbulent flow dynamics stands out from the otherwise regularly-patterned laminar flow region, here characterised by a dislocated arrangement of SPI sustained by the centrifugal instability near the inner cylinder.

A statistically equivalent state can be approximately represented in a much smaller parallelogram-shaped domain. The coordinate change (2.8) can be tailored to choose one of the new coordinates along the statistically-invariant (tilt) direction of the spiral, say ζ by enforcing $n_1/k_1 = \hat{n}/\hat{k} = 5$ for a left-handed spiral as that of figure 1a. If we are to keep the same statistical axial/azimuthal periodicity of SPT we must in fact set $(n_1, k_1) = (\hat{n}, \hat{k}) = (1, 0.2)$. This pair encodes all that is required of a domain to allow for the large-scale structure of SPT, such that we are left with absolute freedom for the choice of the second pair (n_2, k_2). The tilt of the second axis of the parallelogram domain, ξ, will then be given by n_2/k_2, and the volume ratio of the full orthogonal domain to the parallelogram domain is $V_r = k_2/\hat{k} - n_2/\hat{n}$. Figure 1b shows one such domain corresponding to $(n_1, k_1, n_2, k_2) = (1, 0.2, -8, 1.6)$ (thick white parallelogram), which is $V_r = 16$ times smaller than the full orthogonal domain. In the figure, the instantaneous field has been periodically replicated along both the ξ and ζ coordinates, to exemplify how the parallelogram domain relates to the orthogonal domain (white lines tessellation). The instantaneous fields are undoubtedly similar, including the centrifugally driven SPI pattern in
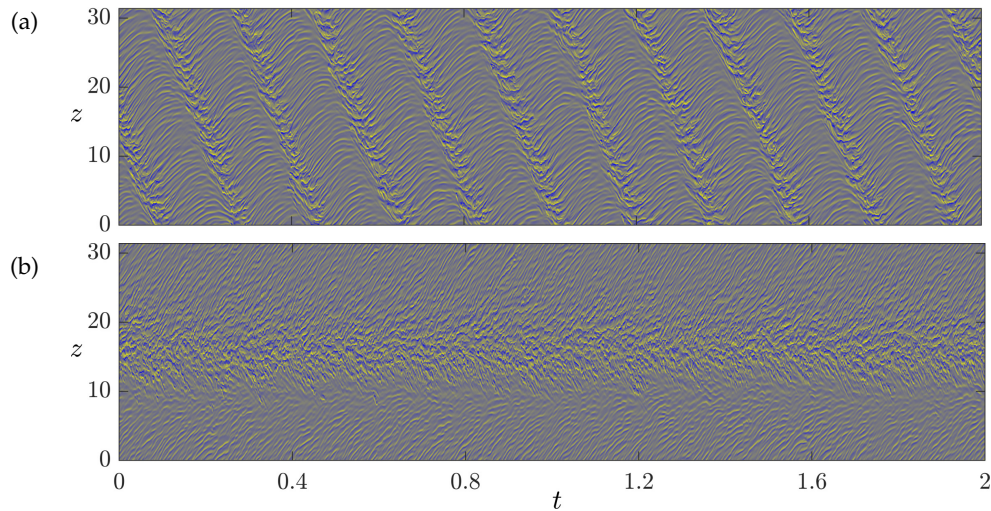
Figure 2. Space-time diagram of radial vorticity $\omega_r(r_{\rm cu}, \theta(t), z; t)$ along an axial probe line in (a) the stationary reference frame with $\theta(t) = 0$, and (b) a reference frame rotating at the instantaneous angular velocity of SPT as obtained from the method of slices, with $\theta(t) = -\Delta\theta_s(t)$ the instantaneous azimuthal drift with respect to the slice template. Colour range as in figure 1.

the quiescent region of the large-scale structure. However, only a rigorous statistical analysis, described in detail in section §4, can genuinely quantify the degree to which the computation in the small parallelogram domain can be considered indistinguishable from that in the large orthogonal domain.

In TCF, the broken symmetries induce a non-trivial angular drift on all non-axisymmetric flow states, including SPT. This drift of SPT is clearly visible in the space-time diagram of figure 2a. Computing statistics of local quantities in the stationary frame of reference would result in averaging the laminar and turbulent regions together, and the essence of intermittency would be lost the process. Preserving the localised structure of SPT thus requires special care in defining a suitable rotating frame of reference. In order to compute field statistics in a co-rotating frame, Dong [6] estimated the average drift speed from a velocity point probe employing Fourier analysis. This method crucially depends on the instantaneous drift being nearly constant, drift speed fluctuations resulting in the undesired smearing out of the average fields. Here we opt instead for using the instantaneous drift speed to avoid the blurring effect. This can be done unambiguously by quotienting out the drift along the group orbit associated with continuous rotation through the slicing technique [19], which renders the statistically converged fields unique but for the (somewhat arbitrary) choice of the slice template (see appendix A in supplementary materials). The template must of course capture the large-scale features of SPT so that the instantaneous drift speed of the rotating reference frame effectively fixes the solution and field statistics can be computed in a meaningful way and with sufficient sharpness. Figure 2b shows the same space-time diagram of 2a, but obtained in the reference frame rotating with the instantaneous angular speed of SPT as computed with the method of slices.

All cases run here but one have used a simple slice template with $a_{011}^{(1)} = 1.0$ (equivalently $a_{111}^{(1)} = 1.0$ for the full orthogonal domain) and all other expansion coefficients set to exactly 0.0. This corresponds to a pure oblique/spiral mode with the same tilt as SPT and a purely radial-azimuthal velocity field. A single run for the case $(n_2, k_2) = (-8, 1.6)$, i.e $V_r = 16$, $n_2/k_2 = -5$, with $(L, N, M) = (30, 240, 24)$, $\Delta t = 8 \times 10^{-6}$, and the template $a_{011}^{(2)} = 1.0$, corresponding to a spiral-like distribution of azimuthal-axial velocity, has been performed for comparison.

Despite the two templates being essentially different, integral deviations remain below 1% for both velocity and Reynolds stress fields, regardless of whether individual components or vector/tensor norms are used in the comparison. The statistical flow fields seem therefore robust to the choice of slice template. In section §5, we will examine the flow field topology of the statistically converged mean SPT regime in detail.

4. Statistical and numerical convergence

The spatio-temporally chaotic nature of the SPT regime requires that convergence be analysed from a statistical standpoint. We will be employing first and second order moments of turbulent signals and field variables as a means of quantifying the inaccuracies associated with domain shape, size and space discretisation.

All simulations were run for a minimum of 20 to 40 viscous time units past all foreseeable transients until a statistically steady turbulent state had been reached. Statistics were then collected over an additional 40 to 100 viscous time units, depending on domain size. The expected statistical invariance of SPT along the spiral coil allows for a final averaging of already time-averaged flow fields in this direction. As a consequence, the degree of convergence is not an increasing function of just the total time-integration lapse T, but of its product with the aspect ratio Λ of the domain, namely $T\Lambda$. Accordingly, a simulation in a domain double the aspect ratio, requires, in principle, half the integration time for a comparable degree of convergence accuracy.

Signal stationarity, i.e. the absence of coherent trends on time scales longer than the simulation time span, is an essential requirement for the obtention of meaningful and reliable statistics. The augmented Dickey-Fuller test [25,26] was performed on all individual production data sets to check for stationarity. The null hypothesis that a unit root is present in the time series sample was rejected with over 99.999% confidence in all cases, implying that no long term trends pointing at the presence of transients could be inferred from any of the signals. The mean and rms of the fluctuation component (standard deviation) of every signal were computed directly from the time series, and 95% confidence intervals were produced for both estimators using stationary bootstrapping [27] with automatic block size optimisation [28,29].

All postprocessed data of time-series and field statistics used in the evaluation of statistical and numerical convergence is given as supplementary material (Appendix E) for completeness.

(a) Baseline computation in the full orthogonal domain

Figure 3a shows the instantaneous axial-azimuthal modal energy distribution ($E_{\ell n}$) of the instantaneous SPT snapshot of figure 1a as computed in the usual orthogonal domain. The volume-averaged kinetic energy of the perturbation field has been additively decomposed into the sum of the various modal energies following

$$E(\mathbf{u}) = \sum_{\ell=-L}^{L} \sum_{n=-N}^{N} E_{\ell n}, \qquad E_{\ell n} = \frac{1-\eta}{1+\eta} \int_{r_\mathrm{i}}^{r_\mathrm{o}} \mathbf{u}_{\ell n} \cdot \mathbf{u}_{\ell n}^{\dagger} \, r \, \mathrm{d}r, \qquad (4.1)$$

where † denotes complex conjugation. The modal energy is high for the low axial (ℓ) and azimuthal (n) Fourier components of the instantaneous velocity field, but decays fast as higher and higher wave numbers are considered. In order to resolve turbulence to an acceptable degree, the axial and azimuthal resolutions have been set sufficiently high that the modal energy decays by at least six orders of magnitude from the most energetic non-spiral ($\ell \neq n$) mode to the tiniest resolved scales. Note that the decay exceeds the eight orders of magnitude if all modes are considered, thus surpassing the most stringent criterion used in the literature [30]. The red contour delimits the region of the spectrum beyond which the energy decay condition has been accomplished. The particular time instant chosen for the analysis could have been resolved with about $(L, N) \simeq (250, 250) < (324, 324)$.
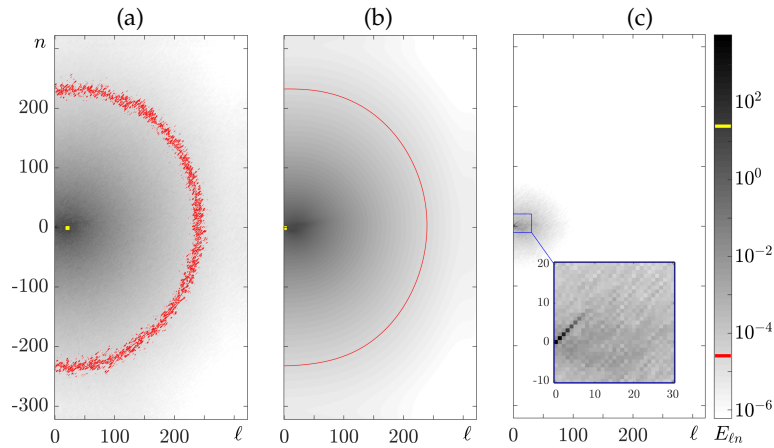
Figure 3. Axial-azimuthal Fourier spectrum of SPT. Modal energy distribution $E_{\ell n}$ colourmaps. (a) Instantaneous spectrum. (b) Time-averaged spectrum. (c) Spectrum of the mean field solution as obtained via the slicing technique. The inset shows a zoom of the squared region. The red line indicates the contour level for six orders of magnitude decay from the highest-energy non-spiral mode ($\ell \neq n$), shown in yellow.

estimator	κ	τ_{i}	τ_{o}	c_θ
$\overline{\bullet}$	0.0855 ± 0.0002	1.657 ± 0.001	1.657 ± 0.002	-34.21 ± 0.07
$\sigma_\bullet = \sqrt{\overline{(\bullet - \overline{\bullet})^2}}$	0.0030 ± 0.0002	0.0200 ± 0.0006	0.0233 ± 0.0007	3.48 ± 0.06

Table 1. Statistics of normalised kinetic energy (κ), normalised inner (τ_{i}) and outer (τ_{o}) cylinder torque, and azimuthal drift speed (c_θ) time signals of SPT in the full orthogonal domain.

To guarantee that the resolution is sufficient throughout the computation, the instantaneous spectrum has been averaged in time (figure 3b) and the variance (not shown) computed employing Welford's online algorithm [31]. Mean and variance combined show that $(L, N) = (\hat{L}, \hat{N}) = (324, 324)$ modes are vastly sufficient to secure the six orders of magnitude decay at all times in the orthogonal domain. Figure 3c shows instead the spectrum of the SPT mean velocity field as obtained using the aforementioned slicing technique. All modes but those unravelling the spatial arrangement of SPT exhibit a decaying trend, the spiral modes clearly sticking out from the background within the low wavenumber region of the spectrum. This attests to an evident preservation of the large-scale structure of SPT when averaging is done in an adequate rotating frame.

The aggregate/integral signals used in assessing the degree of convergence of SPT are the kinetic energy (κ), the inner (τ_{i}) and outer (τ_{o}) torques, and the azimuthal drift speed (c_θ), this latter obtained through the slicing technique. The mean and rms of these scalar time series are the statistical estimators that have mainly been used here to assess convergence.

The time-series statistics for the reference simulation in the full orthogonal domain are given in table 1 for reference. While the mean of all four time signals is converged to within less than 1% with 95% confidence, the uncertainty in rms values is about 3% for c_θ, 6% for $\tau_{\mathrm{i,o}}$ and reaches up to 13% for κ.

In order to dissect the mean structure of SPT and also to quantify deviations upon modifying domain size, shape and resolution in section §4(b), we have computed the slice-averaged velocity ($\overline{\mathbf{u}}$) and Reynolds stress tensor ($\overline{\mathbf{u}' \otimes \mathbf{u}'}$) fields, where $\mathbf{u}' \equiv \mathbf{u} - \overline{\mathbf{u}}$ is the fluctuation component of the velocity field and $\otimes$ denotes the tensor product. By slice averaging, henceforth denoted with an overline, we refer to the sequential application of time averaging in the co-rotating reference
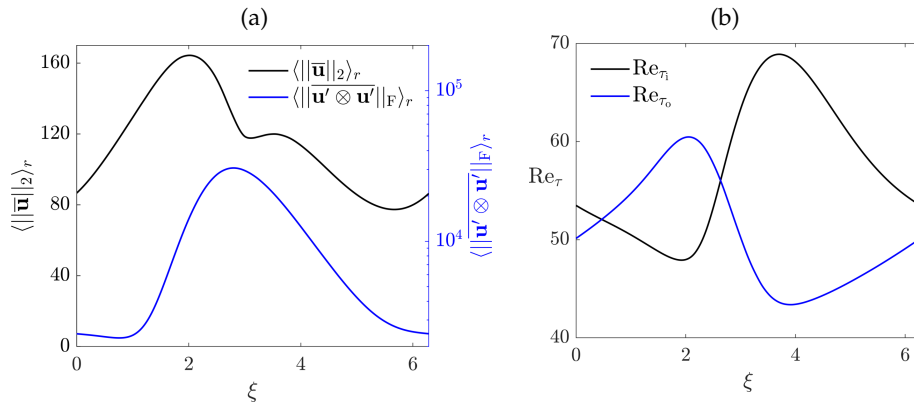
Figure 4. Transverse distributions of slice-averaged flow fields of SPT. (a) Radially-averaged norms of mean velocity ($\langle \|\overline{\mathbf{u}}\|_2 \rangle_r = (\overline{u}_r^2 + \overline{u}_\theta^2 + \overline{u}_z^2)^{1/2}$, L_2 norm) and Reynolds stress tensor ($\langle \|\overline{\mathbf{u}' \otimes \mathbf{u}'}\|_F \rangle_r = (\overline{u_r' u_r'}^2 + \overline{u_\theta' u_\theta'}^2 + \overline{u_z' u_z'}^2 + 2\overline{u_r' u_\theta'}^2 + 2\overline{u_r' u_z'}^2 + 2\overline{u_\theta' u_z'}^2)^{1/2}$, Frobenius norm). (b) Friction Reynolds number Re_τ on the inner and outer walls.

frame defined with the method of slices, followed by further averaging along the invariant spiral direction. This latter spatial averaging requires the prior expression of the time-averaged fields in some parallelogram coordinate system with $\xi = \hat{n}\theta + \hat{k}z$ and arbitrary ζ, so that the ζ-axis is parallel to the spiral. The precise definitions and implementation details of slice averaging are presented in appendix A as supplementary material.

Figure 4a shows the transverse distribution of the radially-averaged norms of the slice-averaged velocity ($\langle \|\overline{\mathbf{u}}\|_2 \rangle_r$, L_2-norm) and Reynolds stress tensor ($\langle \|\overline{\mathbf{u}' \otimes \mathbf{u}'}\|_F \rangle_r$, Frobenius norm) fields. Slice-averaged fields might be equivalently depicted on any plane transverse to the spiral direction on account of the helical invariance of SPT. Here and throughout the paper, we represent all fields (and transverse distributions) as a function of r and the transverse coordinate $\xi \in [0, 2\pi]$. The ξ-axis can be taken as pointing in any transverse direction by defining the ζ coordinate appropriately. In particular, ξ can be interpreted as $\theta \in [0, 2\pi]$ or $z \in [0, \Lambda]$ indistinctly, according to the preference of the reader. The Reynolds stress norm peaks in the middle of the domain and pinpoints the location of the turbulent stripe. The leading and trailing interfaces correspond to the left and right fronts, respectively, as the left-handed spiral winds in the negative θ direction. Turbulent decay is nonetheless far from reaching stationarity. The laminar region retains a considerable level of velocity fluctuations, due to the presence of a pattern of SPI-like solutions (see figure 1 and supplementary movie) that have a differential drift with respect to that of the large-scale SPT. An extended analysis of the flow structure characterising SPT will be undertaken in section §5.

The gap-based friction Reynolds number of the turbulent spiral has been computed a posteriori by evaluating $Re_\tau = u_\tau d/\nu$ at $r = r_i$ or r_o. Here $u_\tau = \sqrt{\tau_w/\rho}$ is the friction velocity, which is obtained from the mean wall shear stress $\tau_w = \mu (r\partial_r(\overline{v}_\theta/r) + \partial_r \overline{v}_z)$. As shown in Figure 4b, the values obtained range in $Re_\tau \in [47.9, 68.9]$ and $[43.4, 60.5]$ for the inner and outer wall, respectively. We shall see in section §5 that the extrema of the Re_τ along each one of the cylinders correspond to the location where the sheared core of the laminar and turbulent regions *touch* the walls. The radial spacing for an equivalent physical grid at the Chebyshev collocation nodes is $\Delta r^+ < 2.5$ across the gap, reducing down to $\Delta r^+ < 0.09$ on the walls. The azimuthal and axial equivalent Fourier spacings are also very well resolved with $\Delta(r\theta)^+ < 5.1$ and $\Delta z^+ < 3.4$.
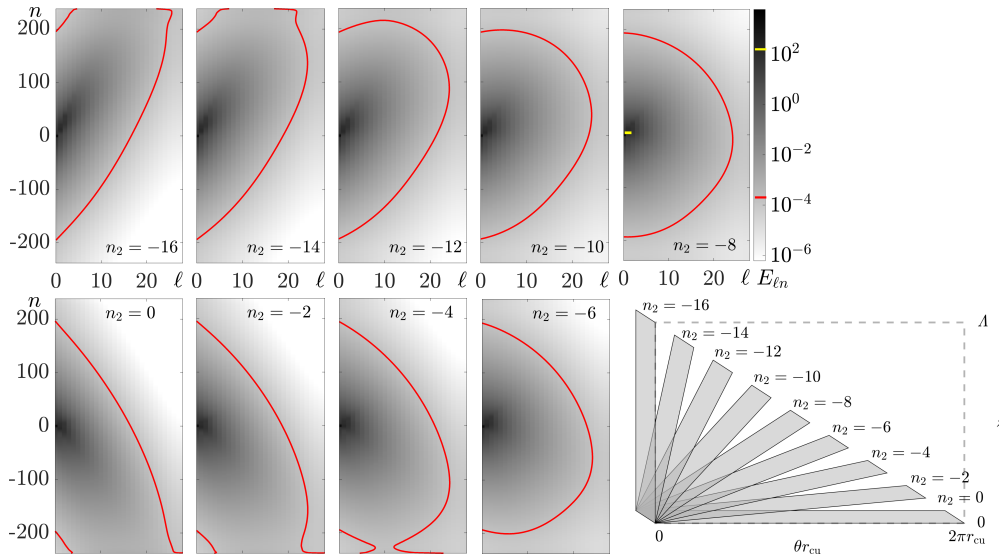
Figure 5. Time-averaged modal energy distribution of SPT as computed in parallelogram domains with $(n_1, k_1) = (\hat{n}, \hat{k}) = (1, 0.2)$, volume ratio $V_r = 16$ and various shapes prescribed by $(n_2, k_2) = (n_2, V_r + n_2/\hat{n})\hat{k} = 3.2 + 0.2n_2$ for $n_2 \in \{-16, -14, -12, -10, -8, -6, -4, -2, 0\}$. The bottom rightmost panel contains a sketch of the parallelogram domain shapes used.

(b) SPT in parallelogram-shaped domains

We proceed next to assess the feasibility of reproducing SPT statistics in parallelogram-shaped domains with the aim of minimising the computational requirements.

First we consider what resolution in the simplest possible parallelogram-shaped domain would be equivalent to a given axial-azimuthal resolution in the full orthogonal domain. The parallelogram $(n_1, k_1, n_2, k_2) = (\hat{n}, \hat{k}, -\hat{n}, \hat{k})$ should in principle be capable of handling SPT of one tilt $(\hat{n}/\hat{k})$ and its opposite $(-\hat{n}/\hat{k})$ with half the volume and, accordingly, half the resolution $L = N = \sqrt{\hat{L}\hat{N}/2} \simeq 230$, which we have rounded up to $(L, N) = (240, 240)$ to make the most of the FFTW routines [32]. For other parallelogram domains, since the transverse (ξ) direction must keep the periodicity of the spiral, we have fixed $N = 240$, while the resolution along the parallel (ζ) direction will be scaled with the domain size to keep an approximately constant resolution density. All in all, we have used $(L, N) = (480/V_r, 240)$, always rounding L to some convenient value. For instance, the parallelogram domain of figure 1b has $V_r = 16$ and, therefore, $L = 30$.

While there is a clear advantage in choosing one of the parallelogram domain sides in the direction of the turbulent spiral, as this alone allows reducing the overall size of the domain (and, with it, the computational burden), it is not obvious that there should be some preference as regards the other side. In order to clarify this, we have run a batch of experiments with varying transverse tilts n_2/k_2, while keeping the parallel tilt at $n_1/k_1 = 5$ and a domain size with $V_r = 16$, i.e. $k_2 = (V_r + n_2/\hat{n})\hat{k} = 3.2 + 0.2n_2$ with $n_2 \in [-16, 0]$. As it happens, the resolution used, $(L, N) = (30, 240)$, is more than enough to resolve SPT with an accuracy such that no effect of domain shape can be perceived on either time-series statistics, or mean velocity or Reynolds stress fields. However, the average spectra of figure 5 clearly show that the choice for the second coordinates does indeed matter. The $(n_2, k_2) = (-8, 1.6)$ run, the one that has $n_2/k_2 = -n_1/k_1 = -\hat{n}/\hat{k} = -5$, is optimal in the sense that the threshold for the six orders of magnitude decay in modal energy (red contour line) has no bias toward positive or negative n. As n_2/k_2 is modified away from this value, the energy decay threshold loses its symmetry to one

or the other side and hits the $+N$ or $-N$ boundary. We can therefore expect that the resolution in the $n_2/k_2 = -5$ case may be safely reduced without crucially affecting the statistical accuracy, while such a resolution coarsening would be increasingly detrimental for domains approaching a horizontal or vertical tilt. The nature of turbulence within the turbulent stripe provides a plausible explanation for this fact. The high Fourier modes are indeed required to resolve the smallest turbulent structures in the flow. Although the large-scale structure of SPT, along with other smaller-scale coherent structures, introduces a certain degree of axial disymmetry in turbulent fluctuations, the axial-azimuthal cross-correlations seem to remain quite impervious at the tiniest scales. As a result, a mesh that preserves the mirror symmetry about $r - \theta$ plane seems to work best, and this is achieved with $n_2/k_2 = -n_1/k_1$ and an adequate resolution.

While the convergence of Fourier expansions along periodic coordinates can be readily assessed through the modal energy decay rule, the radial Chebyshev resolution requires explicit appraisal. We find that $M = 24$ modes are sufficient to keep deviations with respect to full radial resolution ($M = 42$) within statistical accuracy (see appendix B in supplementary material). Besides, the means of the inner and outer torques agree to within statistical accuracy (the radial flux of azimuthal momentum must be conserved on average), which indirectly validates both the spatial resolution and time sample length used [30]. Regarding time integration horizons, $T = 40$ to 100 time units as have been used in the bulk of the numerical experiments performed are sufficient to drop the level of uncertainty in the estimation of time series mean below 1.3% (with 95% confidence). The estimation of rms, however, typically exceeds 5% and sometimes even reaches beyond 10%. Results show that extending the time integration from $T = 100$ to 1000 takes relative uncertainties in the mean below 0.5% and rms estimation can be trusted to within 2.5%, which is not a large gain for a 10-fold increase in computational time (see appendix C in supplementary material). Statistics of SPT, particularly rms, require very long time series for convergence so that a minimal parallelogram domain offers a clear benefit.

We next turn our attention to the effects of domain size on time series statistics. Following the averaging properties of normalised aggregate/integral time signals as we are using here, fluctuation amplitudes are expected to vanish in the limit of an apparatus of infinite aspect ratio. For finite aspect ratio, fluctuation amplitude is therefore dependent on domain size and signal variance is expected to scale inversely with the size of the domain along the spiral direction, provided that the distance is long enough for flow structures to sufficiently decorrelate. All signal variances have been accordingly scaled to the reference domain with $\Lambda = 2\pi/k = 31.42$ so as to allow comparison. The deviation of signal mean and scaled variance from asymptotic saturation as the domain size is increased quantifies the adequacy of the domain to allow for sufficient flow decorrelation and, therefore, for properly capturing SPT. We define the relative accuracy for a statistical estimator e as $\varepsilon_a(e) = |1 - \overline{e}/(e_{\max}^{95} - e_{\min}^{95})|$, where $\overline{e}$ is the estimator mean and $e_{\min}^{95}$ and $e_{\max}^{95}$ the lower and upper bounds of the 95% confidence interval as estimated through bootstrapping. We further define the relative deviation error with respect to the reference case R as $\varepsilon_d(e) = |1 - \overline{e}/\overline{e}_R|$. The accuracy can only be improved by extending the time sample, and provides a lower threshold below which deviations cannot be considered statistically significant.

Figure 6 shows relative accuracies and relative deviations of time-series statistical estimators as the domain size is reduced by increasing the volume ratio $V_r = k_2/\hat{k} - n_2/\hat{n} \in [4, 32]$ while keeping $n_2/k_2 = -5$, $(n_1, k_1) = (1, 0.2)$ and $(L, N, M) = (480/V_r, 240, 42)$. Deviations are computed with respect to SPT in the full orthogonal domain $(n_1, k_1, n_2, k_2) = (1, 0.0, 0, 0.2)$, $(L, N, M) = (324, 324, 42)$. Time samples are long enough to keep accuracy of $\overline{\tau}_i$ below $\varepsilon_a(\overline{\tau}_i) < 1\%$ (see figure 6a) while that of σ_{τ_i} oscillates in the range $\varepsilon_a(\sigma_{\tau_i}) \in [5, 10]\%$ (see figure 6c). Accordingly, deviations cannot be considered significant for $V_r \leq 12$ or 16, depending on whether we aim at reproducing the mean (with under 1% error) or the rms (5% error) of $\overline{\tau}_i$. Beyond these values of V_r, the deviations rapidly surge. The statistical estimators of the rest of time series considered ($\overline{\kappa}$, $\overline{\tau}_o$ and $\overline{c}_\theta$) also follow similar trends (see figures 6b,d).

Domain size experiments suggest that flow structures with an axial scale of about $\lambda_z = \Lambda/V_r \simeq 2 \sim 2.6$ play an important role in the statistics. This length scale may be related to
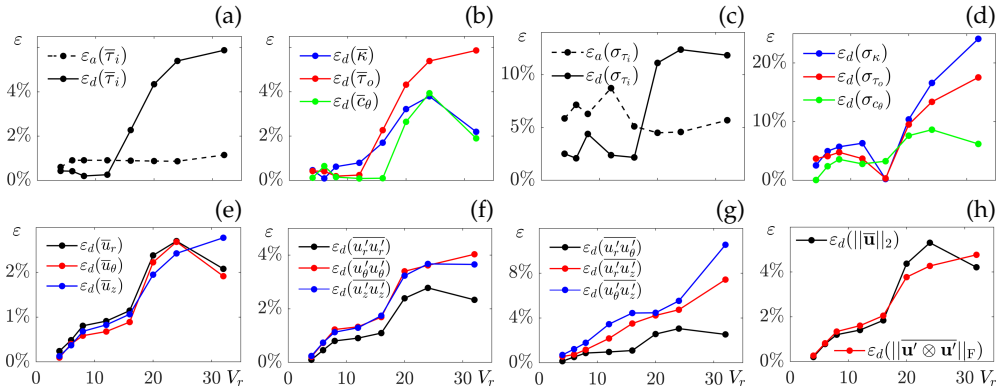
Figure 6. Domain size convergence assessment. For a domain characterised by $(n_1, k_1) = (1, 0.2)$ and $n_2/k_2 = -5$, the volume ratio is varied in the range $V_r = k_2/\hat{k} - n_2/\hat{n} \in [4, 32]$, while keeping the resolution density constant with $(L, N, M) = (480/V_r, 240, 42)$. The reference case is the full orthogonal domain $(n_1, k_1, n_2, k_2) = (1, 0.0, 0, 0.2)$, $(L, N, M) = (324, 324, 42)$. (a) Relative deviation error ε_d and sample length accuracy ε_a for the mean inner cylinder torque ($\overline{\tau}_i$). (b) Deviation errors for mean normalised kinetic energy ($\overline{\kappa}_i$), mean normalised outer cylinder torque ($\overline{\tau}_o$) and mean azimuthal drift speed ($\overline{c}_\theta$). (c) Same as (a) but for rms (σ_{τ_i}). (d) Same as (b) but for rms (σ_κ, σ_{τ_o} and σ_{c_θ}). Also shown are relative field deviations corresponding to (e) mean velocity components ($\overline{u}_r$, $\overline{u}_\theta$ and $\overline{u}_z$), (f) normal Reynolds stress components ($\overline{u'_r u'_r}$, $\overline{u'_\theta u'_\theta}$ and $\overline{u'_z u'_z}$), (g) shear Reynolds stress components ($\overline{u'_r u'_\theta}$, $\overline{u'_r u'_z}$ and $\overline{u'_\theta u'_r}$), and (h) mean velocity ($\|\overline{\mathbf{u}}\|_2$) and Reynolds stress tensor ($\|\overline{\mathbf{u'} \otimes \mathbf{u'}}\|_F$) norms.

the spanwise size of a typical streak [11]. Given that the rolls have a typical diameter of about the gap size (~ 1), the natural spanwise size of streaks should be about twice the gap. Highly subcritical drifting-rotating waves have been identified in counter-rotating TCF that allegedly participate in the dynamics of SPT [17,33]. Their characteristic axial length scale at onset ($R_i \simeq 350$ for $R_o = -1200$) is around $\lambda_z \simeq 1.4$, but it may widen as the inner cylinder Reynolds number is increased to $R_i = 600$ as we have here. It is therefore plausible that the somewhat larger axial wavelength of the domain required for statistical convergence is a consequence of the nonlinear interaction of a continuum of such states of varying size.

Comparison based on individual aggregate/integral time series statistics is prone to error cancellation, particularly so in extremely inhomogeneous flows such as we have. A point-wise comparison of field data provides a much more reliable basis for convergence analysis (see figures 6e-h). Given a reference computation (subscript R), the volume-averaged deviation from reference for the slice-averaged field f is obtained as $\langle|f - f_R|\rangle_{r\xi}$, where f might be any of the mean velocity components ($\overline{v}_r$, $\overline{v}_\theta$ or $\overline{v}_z$), its L_2 norm ($\|\overline{\mathbf{u}}\|_2$), any of the Reynolds stress tensor components ($\overline{v'_r v'_r}$, $\overline{v'_\theta v'_\theta}$, $\overline{v'_z v'_z}$, $\overline{v'_r v'_\theta}$, $\overline{v'_r v'_z}$ or $\overline{v'_\theta v'_z}$), or its Frobenius norm ($\|\overline{\mathbf{u'} \otimes \mathbf{u'}}\|_F$). See appendix A of supplementary material for the rigorous definition of volume averaging. We define the relative deviation by normalising with the maximum absolute local value the field takes for the reference computation: $\varepsilon_d(f) = \langle|f - f_R|\rangle_{r\xi} / \max_{r\xi}|f_R|$.

Relative field deviations are shown in figures 6e-h taking the full orthogonal domain as the reference. All field deviation trends show a clear degradation of convergence for parallelogram domains $V_r \gtrsim 12 \sim 16$ times smaller than the orthogonal domain.

5. The mean structure of statistically converged SPT

Our numerical simulations yield the three individual components of the sliced-averaged perturbation velocity vector field $\overline{\mathbf{u}}$ and the six independent components of the Reynolds stress tensor field $\overline{\mathbf{u'} \otimes \mathbf{u'}}$ in the usual cylindrical coordinates of TCF (see appendix D in supplementary
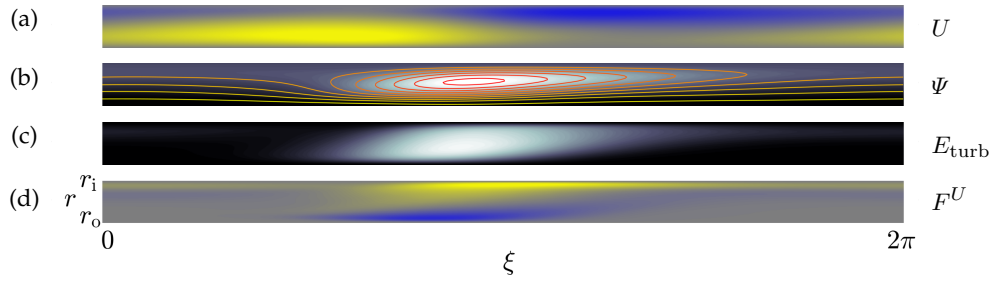
Figure 7. Flow topology of slice-averaged SPT. The colourmaps depict (a) parallel velocity component $U \in [-280, 280]$, (b) streamfunction $\Psi \in [0, 80]$, (c) fluctuation kinetic energy density E_{turb} and (d) Reynolds stress force $F^U \in [-2.5, 2.5] \times 10^4$ in the helically invariant direction. Colour levels increase from blue to yellow and black to white.

material). While providing a general idea of the flow structure of SPT, this projection is not well suited for a detailed examination and full comprehension of the flow mechanisms. We have therefore chosen to project the flow onto a new set of coordinates that is better adapted to capture the structure of SPT in a straightforward manner, as [9] did for PCF.

The helical coordinates of [34] afford a handy and natural description for helically-invariant flows. In this coordinate system, velocity is locally projected onto an orthonormal basis defined by the usual radial axis and two additional axes that are parallel and perpendicular to the direction of spiral invariance. In terms of the notation used by [34], the helically invariant velocity field depends on just the coordinate pair (r, ξ), and its three components are given by (u^r, u^η, u^ξ), where $\eta = a\theta - bz/r^2$ and $\xi = az + b\theta$ are the coordinates parallel and perpendicular to the invariant direction of the spiral, respectively. Notice that the positive η axis points down and rightwards for a left-handed spiral as we have. Following their spiral invariance, slice-averaged fields of SPT can be readily expressed in the helical coordinate system with $a = \hat{k}$ and $b = \hat{n}$. This provides a projection that is amenable to direct comparison with the study by [9] of the laminar-turbulent bands in PCF.

The perturbation velocity components in the helical coordinate system become

$$U = B\left(\hat{k}\overline{u}_\theta - \frac{\hat{n}}{r}\overline{u}_z\right), \quad V = \overline{u}_r, \quad W = B\left(\frac{\hat{n}}{r}\overline{u}_\theta + \hat{k}\overline{u}_z\right), \tag{5.1}$$

where $B(r) = r/\sqrt{\hat{k}^2 r^2 + \hat{n}^2}$. The three helical components have been renamed (U, V, W) in analogy to the PCF analysis of [9], where V is the wall-normal component, and U and W are the components parallel and perpendicular to the stripes, respectively. Actually, the correspondence is exact in the narrow gap limit. Note that the base flow $(U^{\mathrm{b}}, V^{\mathrm{b}}, W^{\mathrm{b}}) = (B\hat{k}v_\theta^{\mathrm{b}}, 0, B\hat{n}v_\theta^{\mathrm{b}}/r)$ must be added to the perturbation velocity when substituting the helical components of total velocity $(u^r, u^\eta, u^\xi) = (U + U^{\mathrm{b}}, V + V^{\mathrm{b}}, W + W^{\mathrm{b}})$ into the helically-invariant Navier-Stokes equations of [34]. According to the mass conservation equation in the transformed coordinates, the radial and perpendicular velocity components can be combined into a streamfunction Ψ satisfying

$$\frac{1}{r}V + \partial_r V + \frac{1}{B}\partial_\xi W = 0 \quad \longrightarrow \quad V = \frac{\partial_\xi \Psi}{r}, \; W = -B\frac{\partial_r \Psi}{r}. \tag{5.2}$$

Following the velocity transformation (5.1), and the definition of the streamfunction (5.2), the velocity field has been visualised in figure 7a,b through its component U in the direction parallel to the spiral (figure 7a), and the streamfunction Ψ (figure 7b) in a unified representation of the two transverse components V and W. The closed streamlines accompanying the Ψ colourmap reveal that a mean anti-clockwise swirl occurs in the midst of the domain. The resulting recirculation bubble moves downward in z and in the negative θ direction (from right to left in the figure) with the spiral as seen from the stationary reference frame. The turbulent kinetic energy $E_{\mathrm{turb}} =$

$\mathrm{Tr}(\overline{\mathbf{u'}\otimes\mathbf{u'}})/2 = (\overline{u'_r u'_r} + \overline{u'_\theta u'_\theta} + \overline{u'_z u'_z})/2$ depicted in figure 7c shows that the core of the turbulent spiral (the white region in the middle) extends over about half the domain periodicity in the transverse direction, indicating that the turbulent and laminar bands are of about the same width. There is a strong correlation between the location of the turbulent core and the mean swirl, which suggests that the transverse perturbation velocity field (represented by Ψ) is mainly driven by turbulence.

The transverse advection induced by the swirling motion spreads the parallel U component of velocity across the full transverse cross-section. The extrema occur precisely at the laminar-turbulent boundaries, which points at a strong component of the mean flow along the spiral fronts. In particular, fluid is, on average, pushed down at the leading edge (left) and pulled up at the trailing edge (right), for a left-handed spiral. The parallel velocity U is the dominant one of the three components, such that both the bimodal distribution of $\langle\|\mathbf{u}\|_2\rangle_r$ in figure 4a and the friction Reynolds number distribution of figure 4b can be explained in terms of it.

The effects of turbulent fluctuations on the conformation of the mean velocity distribution requires a thorough analysis of Reynolds stresses. The mean flow equations of [9] have also their parallel in the helical coordinate system by applying Reynolds averaging to the helically-invariant Navier-Stokes equations derived by [34]. In particular, the momentum conservation equation for the parallel/invariant direction averages to

$$-c_\xi \partial_\xi U \quad = \quad -A^U + D^U - F^U \tag{5.3}$$

$$A^U \quad = \quad V\partial_r(U + U_b) + \frac{1}{B}(W + W_b)\partial_\xi U + \frac{\hat{k}^2 B^2}{r}V(U + U_b) \tag{5.4}$$

$$D^U \quad = \quad \frac{1}{r}\partial_r(r\partial_r U) + \frac{1}{B^2}\partial_\xi^2 U + \frac{\hat{k}^2 B^2(\hat{k}^2 B^2 - 2)}{r^2}U + \frac{2\hat{k}\hat{n}B}{r^2}\left[\partial_\xi V - \partial_r(BW)\right] \tag{5.5}$$

$$F^U \quad = \quad \partial_r\overline{U'V'} + \frac{1}{B}\partial_\xi\overline{U'W'} + \frac{1}{r}\left[1 + \frac{\hat{k}^2 B^2}{r}\right]\overline{U'V'} \tag{5.6}$$

where $c_\xi = \hat{n}\overline{c}_\theta$ is the mean angular drift velocity and $-A^U$, D^U and $-F^U$ represent the advection, diffusion and turbulent forces (the divergence of the Reynolds-stress tensor), respectively. The fluctuation velocity components U', V' and W' in the transformed coordinates are directly obtained from u'_r, u'_θ and u'_z following the rules set by (5.1). Hence, $\overline{U'V'}$ and $\overline{U'W'}$ are easily computed from the Reynolds stress tensor in cylindrical coordinates (shown in appendix D as supplementary material). The distribution of F^U in figure 7d indicates that the turbulent Reynolds stresses that drive U are particularly strong near the cylinder walls.

Comparison of figures 7a-c with the mean structure of the laminar-turbulent patterns of PCF as presented in figure 5 of [9] shows that, despite the slight but evident symmetry-breaking of SPT their overall features are remarkably similar. Parallel turbulent force distribution of SPT, shown in figure 7d, also compares favourably with that for laminar-turbulent stripes in PCF (see figure 14 of [9]). However, for the supercritical counter-rotating regime of TCF, the centrifugally-driven SPI that arise due to the linear instability of CCF leave their distinct imprint on the fluctuation kinetic energy E_{turb} and the parallel turbulent force F^U, which are from vanishing in the laminar region. The velocity fluctuations they induce on account of their differential rotating speed with respect to the large-scale structure of SPT (see figure 1 and supplementary movie) show as a faint elongated band in close proximity of the inner cylinder.

The projections on an annular cross-section of the mean perturbation velocity and Reynolds stress tensor field components in primitive cylindrical coordinates are provided as supplementary material in appendix D.

6. Concluding remarks

We have investigated numerically the statistical properties of the turbulent spiral regime (SPT) in the supercritical parameter region of counter-rotating Taylor-Couette flow. The steady progress

in the numerical analysis of turbulent stripes in PCF can be mainly attributed to the use of suitably tilted narrow computational domains and to the absence of drift. The combined use of parallelogram-shaped domains and the method of slices, as we have illustrated here, seems therefore a necessary step towards carrying the analysis of laminar-turbulent patterns over to both the supercritical and subcritical SPT regimes of TCF.

Besides computing the supercritical SPT regime in the best-resolved simulations to date, we provide a detailed characterisation from a statistical perspective. Long time series of aggregate/integral quantities such as normalised kinetic energy (κ), inner (τ_i) and outer (τ_o) cylinder normalised torques, and azimuthal drift speed (c_θ) have been employed in the characterisation. In particular, the mean and rms of fluctuations have been assessed and 95% confidence intervals provided by means of stationary bootstrapping. Further, the statistical flow topology of SPT has been determined by computing mean velocity and Reynolds stress fields in a frame of reference rotating at the instantaneous angular velocity of the turbulent spiral. This has been done via the slicing technique, which unambiguously eliminates the phase drift along the group orbit associated with continuous rotation. The rotating frame is unique but for the slice template (the reference flow field) used in defining it. Nevertheless, we have found that the method is robust as long as the template has a structure that is sufficiently representative of the mean flow field of SPT. If this condition is met, replacing the template does not significantly affect statistical field results.

In the search for computational economy, we have further exploited the statistical invariance of SPT along the direction of the spiral tilt to implement a coordinate transformation that replaces the ordinary periodic orthogonal-annular domain with a periodic parallelogram-annular domain. By aligning one of the new coordinates with the slope of the turbulent spiral band (parallel) and setting the periodicity of the other (transverse) to retain the natural azimuthal periodicity of the pattern, we find that the periodic size of the computational domain can be greatly contracted along the spiral coordinate direction without significantly compromising the statistical properties of SPT.

Altogether, a parallelogram-annular domain $(n_1, k_1, n_2, k_2) = (1, 0.2, -8, 1.6)$, $V_r = 16$ times smaller than the usual orthogonal domain and with periodic coordinates aligned with the turbulent spiral $n_1/k_1 = 5$ and the opposite sign spiral $n_2/k_2 = -5$, provide an optimal choice for computing supercritical SPT at $(R_i, R_o) = (600, -1200)$ in an apparatus with $\eta = 0.883$. Reliable statistics can be recovered with remarkable accuracy with a resolution $(L, N, M) = (30, 240, 24)$, although lower resolutions might still be sufficient in the Fourier directions. This domain preserves the mean and rms of normalised kinetic energy, inner and outer cylinders normalised torque, and azimuthal drift speed time series within 1% and 5%, respectively. The minimal size of the domain appears to be limited by both the wavelength of the turbulent spiral band and the cross-stream width of the typical streaks. While the orientation of the transverse coordinate may be chosen arbitrarily, the apparent statistical axial symmetry of the tiniest turbulent scales seem to favour slopes of the same magnitude but opposite tilt as that of the parallel (or spiral) coordinate.

In order to expose the mean structure of SPT, flow field statistics have been collected on a suitably rotating frame of reference defined through the method of slices [18,19]. The characteristic statistical invariance in the spiral direction has been exploited to enhance convergence by further averaging along the helical coordinate. Deviations in the norms of the mean perturbation velocity and the Reynolds stress tensor fields for the optimal parallelogram domain with respect to the full orthogonal domain are below 1% and 2%, respectively.

The mean flow topology reveals a distinct spiral structure, while the Reynolds stress fields evince the localised nature of turbulent fluctuations within a well-defined spiral coil. The mean flow structure is most clearly understood in a helical coordinate system [34], which also enables direct comparison with the turbulent stripes in PCF. The qualitative similarity is striking. This is a somewhat surprising result, given that the SPT regime we have analysed belongs in the supercritical region of parameter space, where TCF is subject to centrifugal instability. It appears that centrifugal effects are merely collateral and affect SPT only mildly. As for channel flows, the

natural spacing between consecutive turbulent stripes does not allow for a clear relaxation onto the laminar base flow. In supercritical TCF, however, centrifugally-driven SPI appear in the vicinity of the inner cylinder and leave a slight but discernible signature on the mean structure of SPT.

The method we present dramatically reduces the computational cost of reproducing SPT accurately. This paves the way to producing extremely long data series, which are essential to the computation of higher-order statistics, as well as enabling parameter explorations hitherto unaffordable. Moreover, we trust that dynamical systems theory will amply benefit from the ready access to accurate datasets of SPT. The search for invariant solutions and the determination of Lyapunov exponents are but two prominent examples of useful goals that the use of parallelogram-annular domains in Taylor-Couette flow puts at the disposal of the fluid mechanics community.

References

1. Tuckerman LS, Chantry M, Barkley D. 2020 Patterns in wall-bounded shear flows.
   Ann. Rev. Fluid Mech. **52**, 010719–060221.
2. Taylor GI. 1923 Stability of a viscous fluid contained between two rotating cylinders.
   Phil. Trans. R. Soc. A **223**, 289–343.
3. Coles D, Van Atta CW. 1967 Digital experiment in spiral turbulence.
   Phys. Fluids **10**, S120–S121.
4. Feynman RP. 1964 *Lecture Notes in Physics*, volume 2.
   Reading, MA: Addison-Wesley.
5. Meseguer A, Mellibovsky F, Avila M, Marques F. 2009 Instability mechanisms and transition scenarios of spiral turbulence in Taylor-Couette flow.
   Phys. Rev. E **80**, 046315.
6. Dong S. 2009 Evidence for internal structures of spiral turbulence.
   Phys. Rev. E **80**, 067301.
7. Dong S, Zheng X. 2011 Direct numerical simulation of spiral turbulence.
   J. Fluid Mech. **668**, 150–173.
8. Berghout P, Dingemans RJ, Zhu X, Verzicco R, Stevens RJAM, van Saarloos W, Lohse D. 2020 Direct numerical simulations of spiral Taylor-Couette turbulence.
   J. Fluid Mech. **887**, A18.
9. Barkley D, Tuckerman LS. 2007 Mean flow of turbulent-laminar patterns in plane Couette flow.
   J. Fluid Mech. **576**, 109–137.
10. Tuckerman LS, Barkley D. 2011 Patterns and dynamics in transitional plane Couette flow.
    Phys. Fluids **23**, 041301.
11. Barkley D, Tuckerman LS. 2005 Computational study of turbulent laminar patterns in Couette flow.
    Phys. Rev. Lett. **94**, 014502.
12. Shi L, Avila M, Hof B. 2013 Scale invariance at the onset of turbulence in Couette flow.
    Phys. Rev. Lett. **110**, 204502.
13. Reetz F, Kreilos T, Schneider TM. 2019 Exact invariant solution reveals the origin of self-organized oblique turbulent-laminar stripes.

Nat. Commun. **10**, 2277.

14. Paranjape CS, Duguet Y, Hof B. 2020 Oblique stripe solutions of channel flow.
J. Fluid Mech. **897**, A7.

15. Deguchi K, Altmeyer S. 2013 Fully nonlinear mode competitions of nearly bicritical spiral or Taylor vortices in Taylor-Couette flow.
Phys. Rev. E **87**, 043017.

16. Ayats R, Deguchi K, Mellibovsky F, Meseguer A. 2020 Fully nonlinear mode competition in magnetised Taylor-Couette flow.
J. Fluid Mech. **897**, A14.

17. Wang B, Ayats R, Deguchi K, Mellibovsky F, Meseguer A. 2022 Self-sustainment of coherent structures in counter-rotating Taylor–Couette flow.
J. Fluid Mech. **951**, A21.

18. Froehlich S, Cvitanović P. 2012 Reduction of continuous symmetries of chaotic flows by the method of slices.
Commun. Nonlinear Sci. Numer. Simul. **17**, 2074–2084.

19. Budanur NB, Cvitanović P, Davidchack RL, Siminos E. 2015 Reduction of SO(2) symmetry for spatially extended dynamical systems.
Phys. Rev. Lett. **114**, 084102.

20. Andereck CD, Liu SS, Swinney HL. 1986 Flow regimes in a circular Couette system with independently rotating cylinders.
J. Fluid Mech. **164**, 155–183.

21. Meseguer A, Mellibovsky F, Avila M, Marques F. 2009 Families of subcritical spirals in highly counter-rotating Taylor-Couette flow.
Phys. Rev. E **79**, 036309.

22. Jiménez J, Moin P. 1991 The minimal flow unit in near-wall turbulence.
J. Fluid Mech. **225**, 213.

23. Hamilton JM, Kim J, Waleffe F. 1995 Regeneration mechanisms of near-wall turbulence.
J. Fluid Mech. **287**, 317–348.

24. Meseguer A, Avila M, Mellibovsky F, Marques F. 2007 Solenoidal spectral formulations for the computation of secondary flows in cylindrical and annular geometries.
Eur. Phys. J. Special Topics **146**, 249–259.

25. Dickey DA, Fuller WA. 1979 Distribution of the estimators for autoregressive time-series with a unit root.
J. Am. Stat. Assoc. **74**, 427–431.

26. Dickey DA, Fuller WA. 1981 Likelihood ratio statistics for autoregressive time-series with a unit-root.
Econometrica **49**, 1057–1072.

27. Politis DN, Romano JP. 1994 The stationary bootstrap.
J. Am. Stat. Assoc. **89**, 1303–1313.

28. Politis DN, White H. 2004 Automatic block-length selection for the dependent bootstrap.
Econom. Rev. **23**, 53–70.

29. Patton A, Politis DN, White H. 2009 Correction to *Automatic Block-Length Selection for the Dependent Bootstrap*, by d. politis and h. white.
Econom. Rev. **28**, 372–375.

30. Brauckmann HJ, Eckhardt B. 2013 Direct numerical simulations of local and global torque in Taylor-Couette flow up to $Re = 30000$.
J. Fluid Mech. **718**, 398–427.

31. Welford BP. 1962 Note on a method for calculating corrected sums of squares and products.
Technometrics **4**, 419–420.

32. Frigo M, Johnson S. 1998 FFTW: an adaptive software architecture for the FFT.
In *Proceedings of the 1998 IEEE International Conference on Acoustics, Speech and Signal Processing*, volume 3, pp. 1381–1384.

33. Deguchi K, Meseguer A, Mellibovsky F. 2014 Subcritical equilibria in Taylor-Couette flow.
Phys. Rev. Lett. **112**, 184502.

34. Kelbin O, Cheviakov AF, Oberlack M. 2013 New conservation laws of helically symmetric, plane and rotationally symmetric viscous and inviscid flows.
J. Fluid Mech. **721**, 340–366.